PHOTONIC SENSORS / Vol. 16, No. 1, 2026: 9560009

Ultra-Long Ultra-Broadband Distributed Acoustic Sensing With Zadoff-Chu Nonlinear Frequency Modulation and LEAF

Rong TANG, Sijin ZHENG, Yunhe SONG, Zhikai LIU, Tianyu HUA, Shengtao ZOU, Qiang JING, and Yunjiang RAO*

Key Laboratory of Optical Fiber Sensing & Communications (Ministry of Education of the People's Republic of China), University of Electronic Science and Technology of China, Chengdu 611731, China

*Corresponding author: Yunjiang RAO E-mail: yjrao@uestc.edu.cn

Abstract: The performances of fiber-optic distributed acoustic sensing (DAS) systems are fundamentally limited by the trade-off between the sensing distance and response bandwidth (RB), constraining the effectiveness of the DAS for long-haul sensing applications greatly. To break such a limitation, this paper proposes a novel Zadoff-Chu (ZC) based nonlinear frequency modulation (ZC-NLFM) scheme that combines the zero-correlation property of the ZC method with the chirp diversity of NLFM. The generated ZC-NLFM pulses exhibit excellent sidelobe and inter-pulse interference suppression, enabling high-sensitivity DAS demodulation even under low signal-to-noise ratio conditions. Furthermore, by employing the large-effective-area fiber (LEAF) with the lower attenuation, higher stimulated Brillouin scattering threshold, and Raman amplification, a wide-frequency-range, long-distance, and low-noise DAS (WLL-DAS) with high strain sensitivity of 94.34 $\mathrm{p\varepsilon}/\sqrt{\mathrm{Hz}}$ over a wide RB of up to 7 kHz and an ultralong sensing distance of 148 km at the spatial resolution of 10 m is achieved simultaneously. Compared to the conventional DAS, the proposed WLL-DAS achieves a 22-fold increase in the RB over an ultralong distance of >140 km, significantly extending the performance boundary and application range of the DAS.

Keywords: Optical fiber sensing; distributed acoustic sensing; nonlinear frequency modulation

Citation: Rong TANG, Sijin ZHENG, Yunhe SONG, Zhikai LIU, Tianyu HUA, Shengtao ZOU, *et al.*, "Ultra-Long Ultra-Broadband Distributed Acoustic Sensing With Zadoff-Chu Nonlinear Frequency Modulation and LEAF," *Photonic Sensors*, 2026, 16(1): 9560009.

1. Introduction

With the increasing demand for all-weather security monitoring driven by national public safety and defense development, distributed acoustic sensing (DAS) based on optical fibers, with unique characteristics, such as fully distributed sensing, strong resistance to electromagnetic interference, long distance, easy installation, low cost, and high sensitivity, emerged as a core technology in various fields of security and safety monitoring [1–3]. By integrating redundant fiber resources in commercial optical communication networks with the DAS technology, optical fiber communication infrastructure can be transformed into a high-density, large-scale sensing network [4], enabling situational awareness and intelligent analysis as well as decision making for the operational safety monitoring of the critical infrastructure, including urban utility networks [5], road traffic systems [6, 7],

Received: 29 October 2025 / Revised: 11 January 2026

DOI: 10.26599/PhoS.2026.9560009
Article type: Research article

public safety [8], power lines [9–11], oil/gas pipelines [12], and providing the real-time monitoring and early warning for natural disasters [13–17].

It is worth noting that in the aforementioned applications, sensing fibers are often deployed over ultralong distances (>100 km), and the inherent transmission loss of optical fibers significantly compromises the accuracy of event localization and recognition in long-haul DAS applications. The use of low-attenuation fibers, such as the large-effective-area fiber (LEAF), which exhibits reduced nonlinear effects and a higher threshold of stimulated Brillouin scattering, can mitigate power fading and support higher launched power, thereby extending sensing distances [18]. Furthermore, distributed optical amplification [19, 20] and advanced light sources [21] are employed to enhance signal strength, but the fundamental trade-off between the sensing distance and response bandwidth (RB) in the DAS still remains a major challenge to achieve broadband acoustic sensing over ultralong distances [22, 23]. For instance, at a sensing distance of 100 km, the maximum RB of the DAS is limited to approximately 500 Hz. However, in practical scenarios, such as the leakage detection of oil/gas/water pipelines, track defect monitoring of high-speed railways, and discharge monitoring of power lines, the relevant acoustic signals exhibit a broad frequency spectrum – often spanning from the infrasound to the kilohertz level. Therefore, it is important to significantly enhance the RB of the DAS for ultralong sensing applications. The adoption of novel modulation and demodulation schemes is the key to addressing such a challenge [24]. Techniques such as time-gated digital optical frequency domain reflectometry [25, 26], positive-negative frequency division multiplexing [22], time-slot multiplexing [27], and the orthogonal code with corresponding mismatched filters [28] are proposed, which can extend the RB and maintain the signal-to-noise ratio (SNR) of the DAS effectively.

This paper proposes a novel wide-frequency-range, long-distance, low-noise (WLL) DAS technique using the Zadoff-Chu (ZC) [29–31] based nonlinear frequency modulation (ZC-NLFM). By modulating and multiplexing the spectral width and temporal duration of ZC-NLFM pulses, the proposed approach can greatly mitigate the fundamental trade-off mentioned above. The ZC-NLFM can provide a high sidelobe suppression ratio and inter-pulse interference suppression, ensuring the independent demodulation of each pulse and high-quality signal recovery. Furthermore, by combining the wide modulation bandwidth of an electro-optic modulator (EOM) and the high extinction ratio (ER) of an acousto-optic modulator (AOM) with spectrum extraction demodulation (SED), the utilization efficiency of spectral resources is significantly improved, while interference fading in the DAS is suppressed well. Moreover, the LEAF (ITU-T G.654.E) with a higher stimulated Brillouin scattering threshold and lower attenuation, compared with the standard single-mode fiber (SSMF), is utilized to obtain higher launched power and longer transmission and sensing distances by combining with the Raman amplification (RA) [32, 33]. As a result, the proposed technique is experimentally validated over a 148 km fiber link, achieving a 22-fold expansion (~7.04 kHz) in the RB. Such a WLL-DAS significantly extends the performance boundary of the DAS and hence allows the DAS to be applied to those ultralong broadband sensing scenarios mentioned above.

2. Principle

In the conventional single-pulse DAS, the RB is fundamentally limited by the pulse repetition frequency, making it difficult to achieve both long-distance and broadband sensing simultaneously. Meanwhile, the optical signal power launched into the fiber is restricted by the fiber nonlinearity and pulse duration, leading to a trade-off among sensing range, RB, and SNR. To mitigate these limitations, the multi-frequency sub-pulses modulation has been introduced as an effective approach, where multiple sub-pulses are transmitted within each repetition period to realize the spread-spectrum operation, and hence, the extended sub-pulse duration increases the optical signal power and improves the SNR. Furthermore, pulse compression is employed to convert wide pulses into equivalent narrow ones while preserving the signal energy, effectively balancing the spatial resolution (SR) and SNR in the DAS. For the pulse-compression-based DAS, the SR is determined by the effective modulation bandwidth B after matched filtering, given by $\Delta z=c/(2n_{\mathrm{eff}}B)$, where $c\approx3\times10^{8}$ m/s represents the speed of light in vacuum, n_{eff}=1.46 is the intrinsic refractive index of the SSMF. Frequency modulation generally includes non-linear/linear frequency modulation (NLFM/LFM) [34]. Compared with the LFM, NLFM signals employ a deliberately designed nonlinear instantaneous frequency variation, reshaping the spectral energy distribution after matched filtering, thereby achieving enhanced sidelobe suppression while maintaining a comparable bandwidth. As a result, the NLFM offers the improved frequency-band utilization and sidelobe performance [35]. The typical NLFM pulses can be written as

$$s_{\mathrm{NLFM}}(t)=A\omega(t)\exp\{\mathrm{j}[2\pi f_c t+\pi v(t)]\} \quad (1a)$$

$$v(t)=\int_0^t v(\tau)\mathrm{d}\tau \quad (1b)$$

where A represents the pulse amplitude, $\omega(t)$ is a window function, t is time, f_c is the carrier frequency, T is the pulse width, $v(t)$ is the nonlinear frequency modulation function, and τ is the time variable inside the integral. In practice, a window function $\omega(t)$ is often applied to the pulse to further suppress the side lobes. The advantages of the NLFM lie in the fact that by properly designing $v(t)$, it can effectively suppress the sidelobe energy and improve the SNR after matched filtering. Within a single pulse repetition period of the conventional DAS, multiple sub-pulses can be transmitted to expand the effective frequency band:

$$s_r(t)=s_{\mathrm{NLFM}}(t-rT_s),\quad r=0,1,\cdots,R-1 \quad (2)$$

where T_s represents the sub-pulse interval and each sub-pulse occupies a different frequency band; r denotes the sub-pulse index; R is the total number of sub-pulses. Let the sampled time-domain complex envelope of the NLFM sub-pulse be $s(t)$, and its discrete sampling is $s[n]$, where n=0, 1, ···, $N_{\mathrm{FFT}}-1$. Here, N_{FFT} is the number of the fast Fourier transform (FFT) points, usually setting to the number of pulse points or its power of two. The spectrum of the NLFM sub-pulse can be expressed as amplitude-phase decomposition:

$$\begin{aligned}\mathbf{S}[k]&=\mathcal{F}\{\mathbf{s}[n]\}[k]=\sum_{n=0}^{N-1}\mathbf{s}[n]\cdot\exp(-\mathrm{j}2\pi kn/N_{\mathrm{FFT}})\\&=|\mathbf{S}[k]|\cdot\exp\{\mathrm{j}\boldsymbol{\theta}_s[k]\},\quad k=0,1,\cdots,N-1\end{aligned} \quad (3)$$

where $\mathcal{F}\{\mathbf{s}[n]\}[k]$ is the FFT of $\mathbf{s}[n]$, $|\mathbf{S}[k]|$ is the magnitude spectrum, k is discrete frequency index, and $\boldsymbol{\theta}_s[k]$ is the phase spectrum.

Using ZC sequences to weight the phase of R sub-pulses in the frequency domain reduces the cross-correlation interference between the sub-pulses. The ZC sequence is an ideal constant modulus sequence, and the constant modulus property ensures the stable power of the transmitted signal and improves the overall SNR and resolution [36]. Let its length be M, then

$$\mathbf{c}[m]=\exp\left[-\mathrm{j}\frac{\pi qm(m+1)}{M}\right],\ m=0,1,\cdots,M-1 \quad (4)$$

where $\mathbf{c}[m]$ represents the mth complex sample of a ZC sequence, and $|\mathbf{c}[m]|$=1 ensures the constant modulus property; q is an integer that is coprime to M (the root parameter) and used to adjust the speed of phase rotation. Map the phase $\angle z[m]$ of the ZC sequence onto the frequency index $k=0,1,\cdots,N-1$ of each sub-pulse and obtain the frequency-domain phase function $\boldsymbol{\Phi}_{\mathrm{ZC}}[k]$, then the frequency-domain phase factor $P[k]$ is given by

$$\mathbf{P}[k]=\exp\{\mathrm{j}\boldsymbol{\Phi}_{\mathrm{ZC}}[k]\},\quad |\mathbf{P}[k]|=1. \quad (5)$$

Using the ZC sequence for frequency-domain encoding of the NLFM means adding an additional phase rotation to the sub-pulses. When they are concatenated in the frequency domain, that is

$$\mathbf{S}_{N-Z}[k] = |\mathbf{S}[k]| \cdot \exp\{\mathrm{j}[\boldsymbol{\theta}_s[k] + \boldsymbol{\Phi}_{ZC}[k]]\} = \mathbf{S}[k] \cdot \mathbf{P}[k]. \tag{6}$$

The corresponding time-domain signal is

$$\mathbf{s}_{N-Z}[n] = \mathcal{F}^{-1}\{\mathbf{S}_{N-Z}[k]\} = \frac{1}{N}\sum_{k=0}^{N-1}\mathbf{S}_{N-Z}[k] \cdot \exp(\mathrm{j}2\pi kn/N). \tag{7}$$

Since the spectrum is only multiplied by **P**[k], the amplitude spectrum |**S**[k]| is preserved, meaning the power spectrum remains unchanged.

The frequency-domain phase encoding only changes the spectral phase without affecting the amplitude spectrum distribution. Therefore, the energy position of the signal in the frequency domain remains unchanged, and it still possesses the same bandwidth expansion characteristics as the original NLFM. At the same time, inter-pulse interference can be effectively suppressed through inverse phase compensation applied during the matched filtering process at the receiver. The autocorrelation function of the ith sub-pulse is

$$R_{ii}(\tau) = \int |S_0(f - f_i)|^2 |P_i(f)|^2 \cdot \exp(\mathrm{j}2\pi f\tau)\mathrm{d}f \tag{8}$$

where $S_0(f)$ denotes the frequency-domain representation of the original NLFM sub-pulse before phase encoding, $P_i(f)$ denotes the frequency-domain phase encoding function applied to the ith sub-pulse, and f represents the discrete frequency variable. Since the phase encoding is phase-only and satisfies $|P_i(f)|^2 = 1$, the power spectral density of each encoded sub-pulse remains identical to that of the original NLFM signal, i.e., $|S_i(f)|^2 = |S_0(f)|^2$. Therefore, the autocorrelation function is determined solely by $|S_0(f)|^2$.

Since the central frequency offset f_i only introduces the phase rotation in the frequency domain without changing the energy spectrum distribution, the main peaks of the auto-correlation of each sub-pulse remain consistent. When the ZC phase encoding $P_i(f)$ is applied, the phase diversity introduced by the ZC sequence redistributes the cross-correlation energy among sub-pulses, thereby reducing coherent sidelobe accumulation in the multi-sub-pulse reconstruction process.

The cross-correlation of the ith and jth sub-pulses is

$$R_{ij}(\tau) = \int S_0(f - f_i) \cdot S_0^*(f - f_j) \cdot P_i(f) \cdot P_j(f) \cdot \exp[\mathrm{j}2\pi f(\tau + \tau_j - \tau_i)]\mathrm{d}f. \tag{9}$$

Among them, the definition of the spectral overlap degree is

$$O_{ij} = \int |S_0(f - f_i)| \cdot |S_0(f - f_j)| \mathrm{d}f. \tag{10}$$

When $|f_i - f_j| \gg$ the sub-pulse bandwidth B, the spectra hardly overlap and the cross-correlation is consequently very small. At this point, it is necessary to set $|f_i - f_j|$ to be greater than $B+\Delta f_{\text{guard}}$, where Δf_{guard} represents the frequency interval between sub-pulses. Furthermore, the dispersion in the optical fiber may introduce frequency shifts into adjacent frequency bands, thus requiring more frequency redundancy to resist inter-pulse interference.

When $|f_i - f_j| \le B$, the spectral overlap and the cross-correlation are mainly determined by the phase. In the ZC-NLFM pulses, the $P_i(f)P_i^*(f)$ value is equivalent to introducing the pseudo-random phase into the overlapping area, where $P_i^*(f)$ is the complex conjugate of $P_i(f)$, dispersing the cross-correlation energy, and ensuring that different sub-pulses still have a relatively low cross-correlation even under high overlapping conditions. At this point, the cross-correlation is abbreviated as

$$|R_{ij}(\tau)| \le O\left(\frac{1}{\sqrt{K_{\text{OV}}}}\right) \tag{11}$$

where K_{OV} represents the number of effective independent phases in the spectral overlap area, approximately representing the de-correlation capability of the ZC method with the advantage of reducing the cross-terms of mutual correlation in scenarios with multiple sub-pulses, thereby further lowering the side-lobe interference, making the side lobe amplitude proportional to $O(1/\sqrt{K_{\mathrm{OV}}})$. Compared with the conventional sidelobe or cross-correlation suppression methods that rely on windowing [26], mismatched filtering or orthogonal time/frequency multiplexing [28], the proposed ZC-NLFM scheme exploits the intrinsic zero-correlation property of ZC coding to simultaneously suppress sidelobes and inter-pulse interference without sacrificing the pulse-compression gain, which is particularly suitable for the dense multi-sub-pulse DAS operation.

In the conventional DAS, the sensing range L and RB are constrained by the pulse repetition period T_r:

$$T_r \geq \frac{2n_{\mathrm{eff}}L}{c} \tag{12a}$$

$$\mathrm{RB} \leq \frac{1}{2T_r} \tag{12b}$$

which leads to an inherent trade-off between the long sensing distance and wide RB. In the proposed WLL-DAS, this limitation is mitigated by employing the multi-sub-pulse ZC-NLFM. Within a single system repetition period T_r, multiple sub-pulses are transmitted and independently demodulated owing to the zero-correlation property of ZC encoding and pulse compression. As a result, the effective RB is determined by the number of transmitted sub-pulses R, given by

$$\mathrm{RB} \approx R\frac{1}{2T_r} \tag{13}$$

while the sensing distance is still governed by T_r and remains unchanged. Therefore, the RB can be significantly expanded without reducing the sensing distance. This decoupling mechanism enables the simultaneous ultra-long sensing distance and ultra-broadband response in the proposed WLL-DAS.

The ZC-NLFM pulses generated are shown in Fig. 1(a), within each system repetition period T_r, R sub-pulses with the equal duration T are transmitted. Among them, one sub-pulse (P_{WB}) is designed with a wide modulation bandwidth, serving as the main pulse to provide the primary compression bandwidth, enhance the spatial resolution (SR), and ensure accurate demodulation and localization in the DAS. The achievable SR is determined by the modulation bandwidth according to $\Delta z=c/(2n_{\mathrm{eff}}B)$, where B is the effective frequency sweep bandwidth of the transmitted pulse. Therefore, a larger bandwidth results in a finer SR. In practical operation, P_{WB} can be segmented into V narrower-band spectrum components through spectrum extraction demodulation (SED), allowing the effective SR to be flexibly tailored to the sensing requirement. These sub-pulses are then coherently combined via rotational vector summation (RVS) to improve the overall SNR. Accordingly, the design of P_{WB} is jointly determined by the required SR and the number of sub-pulses used in the RVS. The remaining R–1 sub-pulses (P_{NB}) are designed with narrower bandwidths and are used to extract dynamic perturbation information. Figure 1(b) presents the schematic diagram of high-frequency signal reconstruction in the DAS based on multi-sub-pulses demodulation. By staggering the sub-pulses in both time and frequency domains, the received signals can be separated through matched filtering or correlation, and subsequently combined to synthesize an equivalent pulse with an extended frequency range. This process enables the reconstruction of the dynamic strain distribution and expands the overall RB of the DAS by a factor of R.

Figures 1(c)–1(e) show the spectrum and auto-correlation characteristics of the ZC-NLFM. As shown in Fig. 1(c), the ZC-NLFM exhibits the same spectrum characteristics as the NLFM, with only slight phase fluctuations introduced by the ZC modulation. In Figs. 1(d) and 1(e), the auto-correlation characteristics of the NLFM and

ZC-NLFM pulse signals with a bandwidth B=10 MHz and duration T=40 μs are presented. After matched filtering, the ZC-NLFM waveform exhibits excellent out-of-band suppression, achieving an 8 dB improvement in the sidelobe suppression ratio compared with that of the NLFM signal, while maintaining a comparable main lobe width.

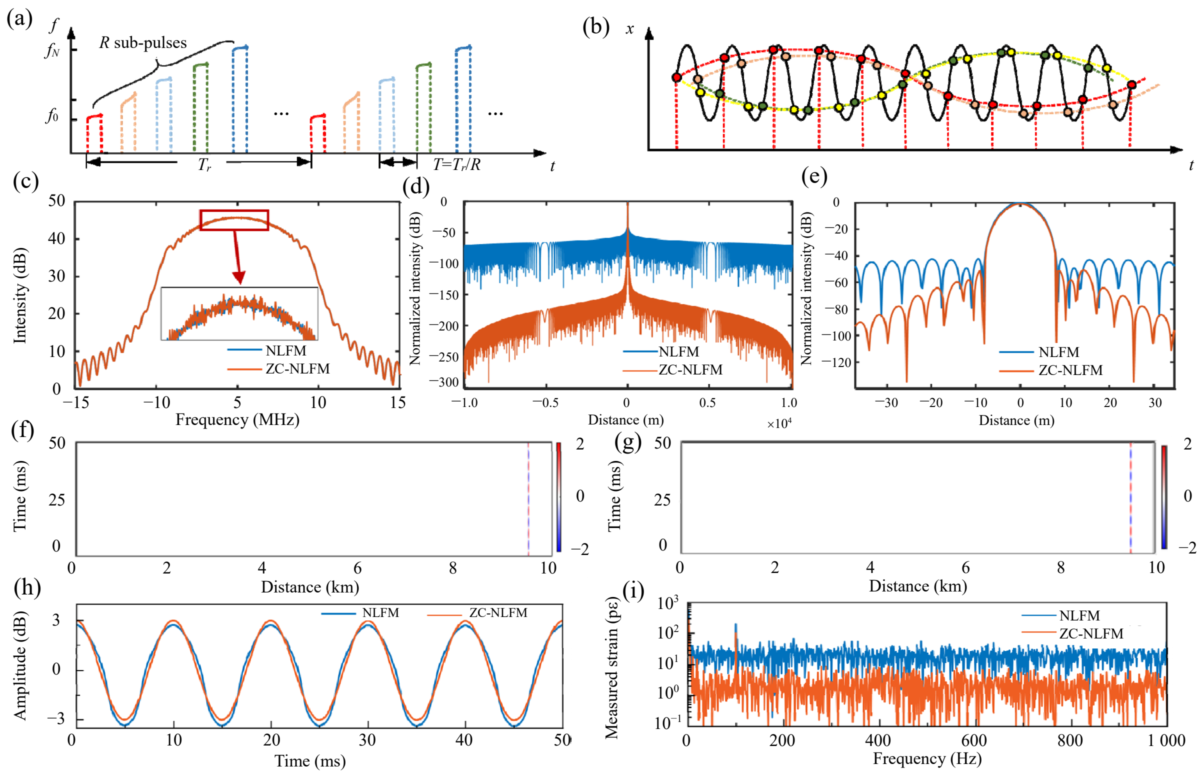

Fig. 1 ZC-NLFM-based DAS: (a) ZC-NLFM pulses, (b) high-frequency dynamic strain signal reconstruction process, comparison of (c) frequency spectrum, (d) autocorrelation characteristics, (e) main lobe width between the NLFM and ZC-NLFM, and the time-distance map of the demodulation DAS signal based on (f) the NLFM and (g) the ZC-NLFM, (h) time-domain waveforms, and (i) power spectral density (PSD) corresponding to the two modulations.

DAS simulations are carried out based on both NLFM and ZC-NLFM modulations, respectively. A 100 Hz electrical sinusoidal signal with an amplitude of 280 nε is applied to a piezoelectric ceramic transducer (PZT) located at 9.5 km along a 10 km fiber to simulate the dynamic strain. Figures 1(f) and 1(g) show the time-distance maps of the demodulated DAS signals based on both the NLFM and ZC-NLFM, respectively, where the disturbance can be clearly observed. Figure 1(h) presents the corresponding time-domain waveform in the disturbed region, which closely matches a standard sinusoidal signal. The PSD of the strain signal is shown in Fig. 1(i). Under these conditions, the PSD noise floors of the NLFM- and ZC-NLFM-based DAS are −58.6 dB·rad^2/Hz and −65 dB·rad^2/Hz, respectively, corresponding to minimum detectable strains of 12.7 $\text{p}\varepsilon/\sqrt{\text{Hz}}$ and 6.1 $\text{p}\varepsilon/\sqrt{\text{Hz}}$.

3. Experiment

3.1 Experimental setup

The experimental setup of the WLL-DAS is shown in Fig. 2. The continuous wave output from a 1 550 nm laser with a linewidth <100 Hz is split into two branches. The upper branch is modulated by an EOM to generate the carrier-suppressed double-sideband ZC-NLFM pulses, and then chopped synchronously by an AOM (Δf=80 MHz). The EOM is driven by an arbitrary waveform generator (AWG). After amplification by an erbium-doped fiber amplifier (EDFA) with a band-pass filter (BPF), the polarization state is controlled by a polarization controller (PC), and the optical power is adjusted by a variable optical attenuator (VOA), and then the final pulses enter the fiber under test (FUT) through a circulator. In this experiment, the FUT is a LEAF with a loss of 0.16 dB/km. Compared to the SSMF with a 0.18 dB/km loss, the LEAF exhibits lower attenuation and reduced nonlinear effects, allowing optical pulse signals to propagate over longer distances. A 1 455 nm semiconductor laser serves as a Raman pump to enhance the SNR at the far end of the FUT via the forward RA. The Rayleigh backscattering (RBS) signal is heterodyned with the local oscillator (LO) light from the lower branch via the circulator. After photodetection by a 1.6 GHz bandwidth balanced photodetector (BPD), the resulting electrical signal is sampled by an oscilloscope with the 1.562 5 GSa/s sample rate.

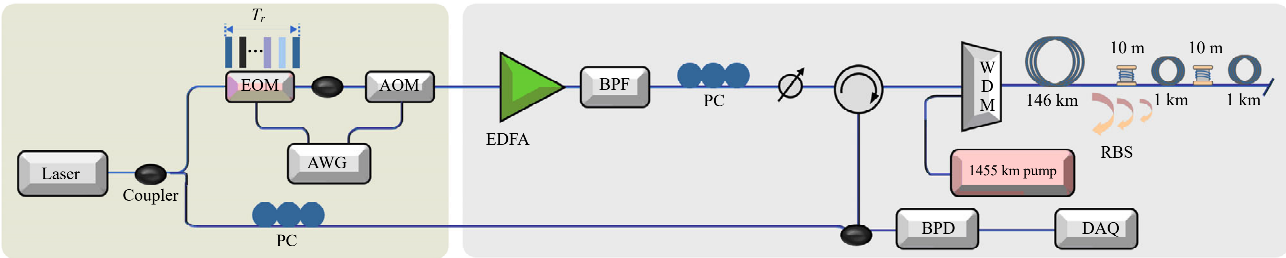

Fig. 2 Experimental setup of the WLL-DAS (WDM: wavelength-division multiplexing; DAQ: data acquisition).

The ultra-wide bandwidth and high-speed modulation capabilities of an EOM are exploited to implement the ZC-NLFM modulation, thereby enhancing the RB and improving the SR. Simultaneously, an AOM is employed to gate the multi-pulses in the time domain, taking advantage of its high ER to extend the sensing distance. Notably, the AOM introduces a frequency shift, which necessitates careful design of the frequency bands for each ZC-NLFM sub-pulse to prevent pulse overlaps among the RBS signals after detection by a BPD due to interference beating effects.

3.2 Experimental results

Considering the BPD bandwidth and the oscilloscope sampling rate, in order to balance the SR and dynamic strain frequency extension range $[0, Nc/4n_{\text{eff}}L]$, while reducing the data processing volume, the system repetition period is selected as T_r=1.562 5 ms, corresponding to a repetition frequency f_s=640 Hz. The number of multiplexed detection pulses R=22, the duration of each pulse T=40 μs, and the interval between adjacent pulses T_r/N=71.023 μs>T. According to (13), the upper limit of the achievable RB expansion of the proposed WLL-DAS scheme is 7.02 kHz. The frequency parameters of the digital ZC-NLFM pulses are designed as Table 1.

The short-time Fourier transform of digital and backward-transmitted ZC-NLFM pulses are shown in Figs. 3(a) and 3(b), respectively. Through the combined effects of double-sideband modulation by the EOM, frequency shifting by the AOM, and coherent detection, the ZC-NLFM signals exhibit an expanded set of usable spectral components. As shown in Fig. 3(b), the digital sub-pulses are arranged into multiple parts. And within each part, the signals are jointly modulated by the EOM and AOM to generate symmetric double-sideband spectra. After beat detection in coherent reception, the sideband components introduced by the EOM modulation are mapped to exactly fill the pre-allocated spectral slots in the digital modulation stage, thereby maximizing the utilization efficiency of the available frequency resources. Figure 3(c) presents the loss curves of the LEAF and SSMF under long-distance transmission. It can be observed that beyond a transmission distance of 31.33 km, the lower loss of the LEAF becomes dominant, resulting in a higher backscattered signal compared with the SSMF. Consequently, the overall SNR is not degraded but instead benefits from the lower attenuation in long-distance DAS operation. This makes the LEAF particularly suitable for ultra-long-distance sensing scenarios. The power distribution of the RBS signals before and after the RA are depicted in Figs. 3(d) and 3(e). After amplification, the SNR at the fiber end increases to 7.6 dB, which is sufficient to enable reliable phase demodulation along the entire 148 km fiber link.

To test the system's ability for synchronized strain measurement at multiple locations, a sinusoidal dynamic strain signal with a frequency of 100 Hz and a voltage amplitude of 5 V (800 nε) is applied to PZT1 and PZT2. The SED with V=6 (the number of spectral segmentation extracts) and rotational vector summation are applied to the wideband frequency component P_{WB}, resulting in a final pulse compression signal with a temporal width corresponding to the reciprocal of 20 MHz. This effective bandwidth corresponds to an SR of 10 m, which is intentionally matched to the 10 m fiber length wound around each PZT to ensure accurate demodulation.

Table 1 Frequency parameters of the digital ZC-NLFM pulses (N=22).

	f_0 (MHz)	Pulse bandwidth (MHz)	Frequency interval (MHz)	f_{max} (MHz)
Part 1 (N_1=5)	5	10	2	65
Part 2 (N_2=1)	228	120	3	351
Part 3 (N_3=3)	351	10	2	387
Part 4 (N_4=13)	547	10	2	703

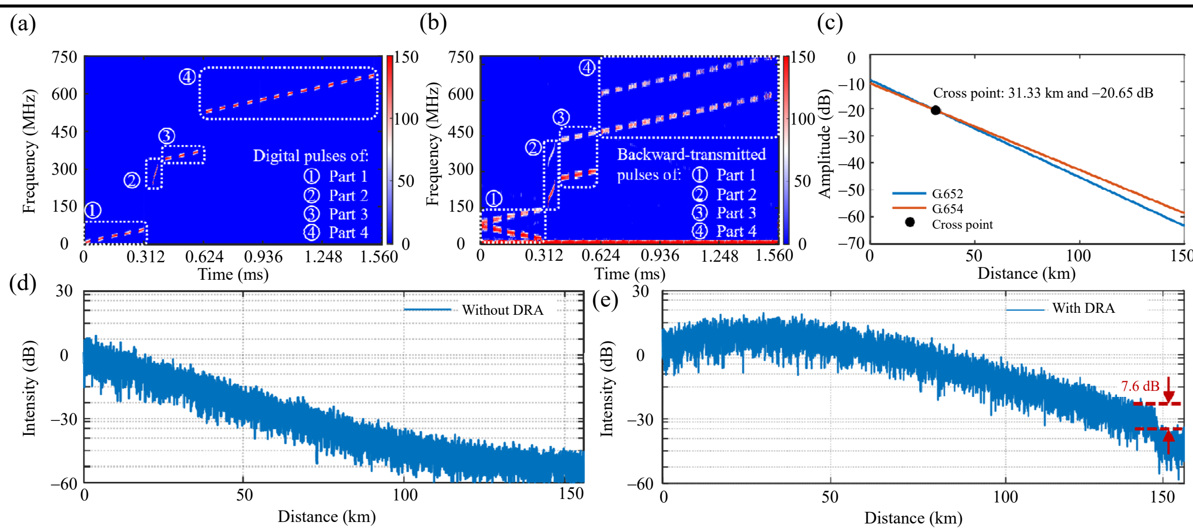

Fig. 3 Characteristics of (a) digital and (b) backward-transmitted ZC-NLFM pulses, (c) simulated attenuation curves of the LEAF and SSMF over long-distance transmission, and the normalized intensity distribution of the RBS signals (d) without and (e) with distributed Raman amplification (DRA).

Figure 4(a) presents the time-distance map of the differential phase at the fiber end, while phase variations in non-dynamic strain regions remain minimal as the interference fading is effectively suppressed. The time-domain waveforms corresponding to the two dynamic strain regions are shown in the inset of Fig. 4(a). A three-dimensional PSD along the optical fiber is presented to further evaluate the crosstalk along the optical fiber, as shown in Fig. 4(c). It can be observed that only significant phase changes occur near the dynamic strain region, while the overall crosstalk along the optical fiber remains very low. Due to the viewing angle of the plotted data, the PSD signals of the two PZTs overlap in the figure. Figure 4(b) presents the standard deviation (STD) of the differential phase at the fiber end, from which the SR of PZT1 and PZT2 can be identified 10 m. Figure 4(d) shows the PSD curves of the system at 100 Hz, where a sensing noise floor below −40 dB rad^2/Hz is achieved.

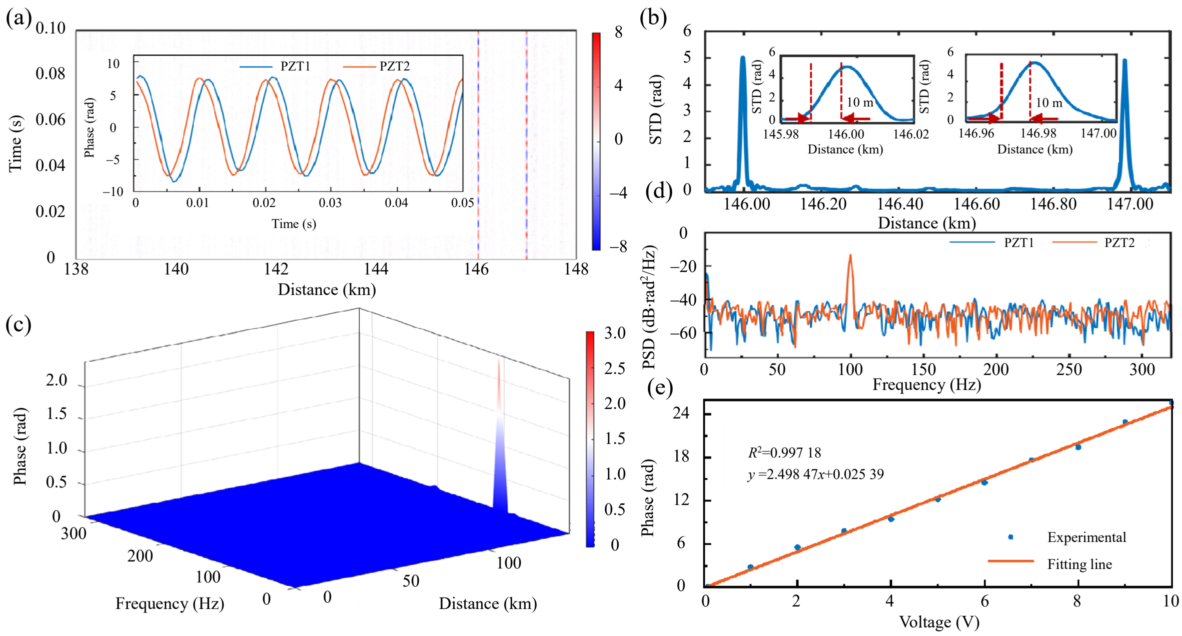

Fig. 4 Phase demodulation results: (a) time-distance diagram of differential phase at the fiber end, (b) STD of differential phase at the fiber end, (c) three dimensional (3D) time-distance diagram of differential phase along optical fiber, (d) PSD of two PZTs, and (e) strain response of PZT1.

To evaluate the system's strain response, sinusoidal dynamic strain signals with a constant frequency of 100 Hz and varying peak-to-peak voltages ranging from 0.1 V to 10 V are applied to PZT1. The measurement results and linear fitting curves are shown in Fig. 4(e). It can be observed that the measurement data for PZT1 closely match the linear function R^2=0.997 18 with a slope of 2.498 47 rad/V. This indicates that the proposed system exhibits good linear response characteristics to external dynamic strains.

Figures 5(a)–5(d) show the high-frequency dynamic strain response signals reconstructed by 22 pulses, under sinusoidal dynamic strains applied to the PZT1 at frequencies of 50 Hz, 3.1 kHz, 4.8 kHz, and 7 kHz, respectively, with a peak voltage amplitude of 4 V. For complex or broadband acoustic signatures, the proposed WLL-DAS scheme reconstructs the dynamic strain by combining the phase-demodulated responses of multiple sub-pulses within a single repetition period. Increasing the number of sub-pulses extends the effective RB, while the associated SNR reduction per sub-pulse can be compensated by using the RVS, LEAF, and DRA. Due to the inconsistent responses of pulses with different frequencies to external disturbances, the intensity of the under sampled low-frequency signals obtained from 22 sub-pulses shows certain amplitude fluctuation. This effect mainly arises from the frequency-dependent phase response mismatch among different sub-pulses. Such amplitude fluctuations can be effectively mitigated by introducing a signal equalization process to compensate for the non-uniform pulse responses [37], thereby improving the signal quality and system robustness. The PSDs of the measured dynamic strain signals with the same voltage amplitude are shown in Fig. 5(e). The SNR of the demodulated signals at each dynamic strain frequency is greater than 30 dB, with a system noise peak of approximately −41.2 dB rad^2/Hz, and the corresponding strain sensitivity is approximately 94.34 $\mathrm{p\varepsilon}/\sqrt{\mathrm{Hz}}$.

Furthermore, we compare the WLL-DAS scheme proposed with the state-of-the-art DAS methods. As summarized in Table 2, the proposed scheme can simultaneously achieve the high strain sensitivity and RB expansion for the long-haul DAS while maintaining the comparable SR.

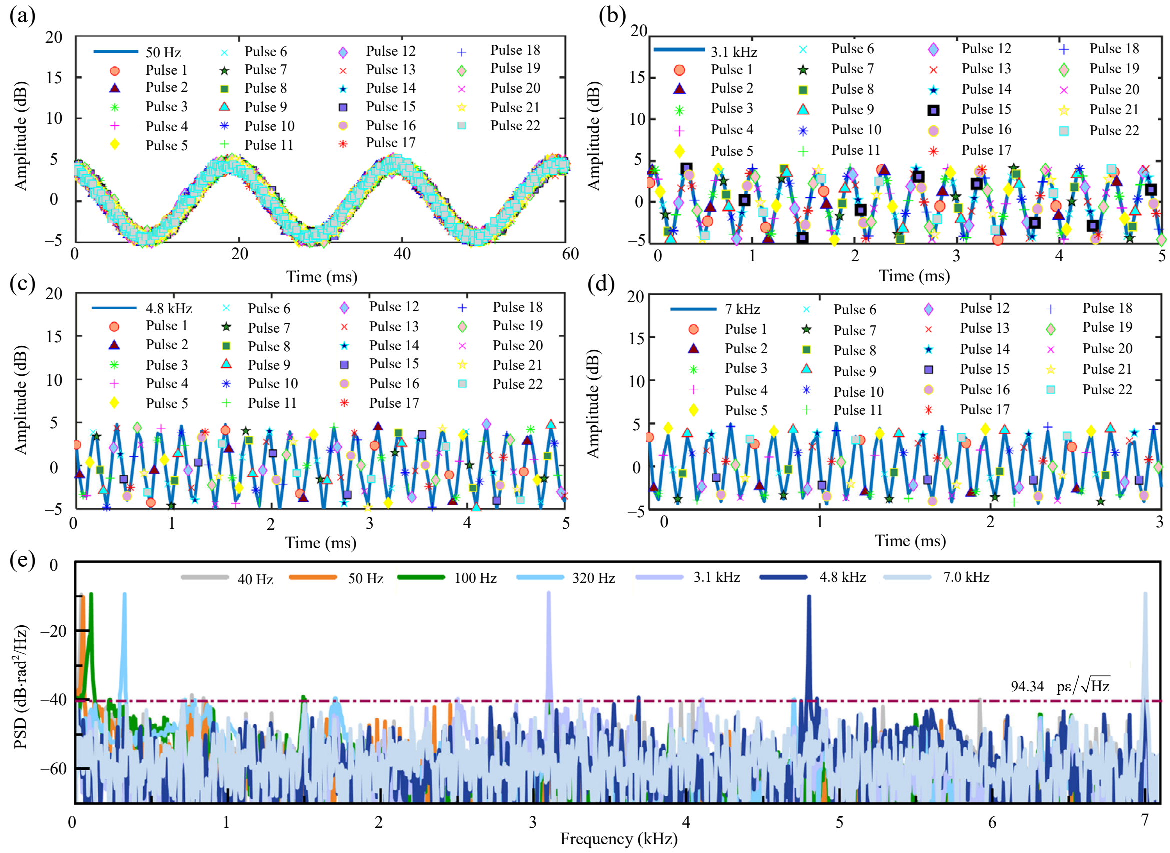

Fig. 5 High-frequency dynamic strain response reconstruction and chirp strain signal demodulation: reconstructed (a)100 Hz, (b) 3.1 kHz, (c) 4.8 kHz, and (d) 7 kHz dynamic strain signal waveforms, and (e) PSD of the measured dynamic strain signals at different frequencies.

Table 2 System performance comparison.

Ref.	Method	Sensing distance (km)	SR	RB extension	Strain sensitivity
[38]	Frequency division multiplexing (FDM) + polyphase coding	21.6	\	5-folds to 10.6 kHz	$83\ \mathrm{p}\varepsilon/\sqrt{\mathrm{Hz}}$
[39]	FDM + dual-frequency-pulse + PM SMF	49.2	\	4-folds to 4 kHz	\
[40]	OFDM+ Vernier effect + weak reflector array	51	\	24-folds to 25 kHz	\
[22]	Negative frequency band + SSMF + DRA	103	9.3 m	24-folds to 10.8 kHz	$97\ \mathrm{p}\varepsilon/\sqrt{\mathrm{Hz}}$
This work	ZC-NLFM + LEAF + DRA	148	10 m	22-folds to 7 kHz	$94.34\ \mathrm{p}\varepsilon/\sqrt{\mathrm{Hz}}$

4. Conclusions

In conclusion, a novel WLL-DAS scheme based on the ZC-NLFM is proposed and experimentally verified. The ZC-NLFM scheme effectively combines the zero-correlation and constant-amplitude properties of the ZC method with the chirp diversity of the NLFM, generating multi-pulses with low sidelobes, strong inter-pulse orthogonality, and high phase demodulation fidelity. This modulation approach significantly enhances signal robustness and suppresses interference in multi-pulses, thereby improving the overall sensing sensitivity. By leveraging the complementary modulation characteristics of the hybrid EOM-AOM architecture and employing the LEAF and Raman amplification, the low-loss, low-nonlinearity, and high-power-tolerant transmission are achieved for ultralong-haul sensing. Experimental results demonstrate a 22-fold enhancement in the RB, reaching 7 kHz over a 148 km sensing distance, representing one of the longest DAS with the widest bandwidth reported to date. This work shows the potential of the proposed ZC-NLFM-based WLL-DAS as a foundation for the realization of next-generation ultra-long ultra-broadband fiber-optic sensing networks for various infrastructure monitoring applications.

Acknowledgment

This work was supported by the Joint Key Funds of the Natural Science Foundation of China (Grant No. U21A20453), and the Basic Research Top Academic Achievement Cultivation Program of University of Electronic Science and Technology of China (Grant No. Y03023206100277).

Declarations

Conflict of Interest Yunjiang RAO is the editor-in-chief for Photonic Sensors and was not involved in the editorial review, or the decision to publish this article. All authors declare that there are no competing interests.

Permissions All the included figures, tables, or text passages that have already been published elsewhere have obtained the permission from the copyright owner(s) for both the print and online format.

Use of AI Statement None.

References

[1] H. Zheng, J. Zhang, N. Guo, and T. Zhu, "Distributed optical fiber sensor for dynamic measurement," *Journal of Lightwave Technology*, 2021, 39(12): 3801–3811.

[2] Y. Rao, Z. Wang, H. Wu, Z. Ran, and B. Han, "Recent advances in phase-sensitive optical time domain reflectometry (Φ-OTDR)," *Photonic Sensors*, 2021, 11(1): 1–30.

[3] T. Liu, H. Li, T. He, C. Fan, Z. Yan, D. Liu, *et al.*, "Ultra-high resolution strain sensor network assisted with an LS-SVM based hysteresis model," *Opto-Electronic Advances*, 2021, 4(5): 200037.

[4] Z. Ran, Y. Rao, L. Luo, Sheng Xiong, and Qiang Deng, "Φ-OTDR used for providing security service in EPON," in *2009 14th OptoElectronics and Communications Conference, IEEE*, Vienna, Austria, July 13–17, 2009, pp. 1–2.

[5] A. Masoudi, J. A. Pilgrim, T. P. Newson, and G. Brambilla, "Subsea cable condition monitoring with distributed optical fiber vibration sensor," *Journal of Lightwave Technology*, 2019, 37(4): 1352–1358.

[6] L. Xie, Z. Li, Y. Zhou, W. Xiang, Y. Wu, and Y. Rao, "Railway track online detection based on optical fiber distributed large-range acoustic sensing," *IEEE Internet of Things Journal*, 2023, 11(4): 6469–6480.

[7] F. Peng, N. Duan, Y. J. Rao, and J. Li, "Real-time position and speed monitoring of trains using phase-sensitive OTDR," *IEEE Photonics Technology Letters*, 2014, 26(20): 2055–2057.

[8] G. Allwood, G. Wild, and S. Hinckley, "Optical fiber sensors in physical intrusion detection systems: a review," *IEEE Sensors Journal*, 2016, 16(14): 5497–5509.

[9] Z. Peng, J. Jian, H. Wen, A. Gribok, M. Wang, H. Liu, *et al.*, "Distributed fiber sensor and machine learning data analytics for pipeline protection against extrinsic intrusions and intrinsic corrosions," *Optics Express*, 2020, 28(19): 27277.

[10] Q. Chai and Y. Luo, "Review on fiber-optic sensing in health monitoring of power grids," *Optical Engineering*, 2019, 58(07): 072007.

[11] Z. Ding, X. Zhang, N. Zou, F. Xiong, J. Song, X. Fang, *et al.*, "Phi-OTDR based on-line monitoring of overhead power transmission line," *Journal of Lightwave Technology*, 2021, 39(15): 5163–5169.

[12] F. Peng, H. Wu, X. H. Jia, Y. J. Rao, Z. N. Wang, and Z. P. Peng, "Ultra-long high-sensitivity Φ-OTDR for high spatial resolution intrusion detection of pipelines," *Optics Express*, 2014, 22(11): 13804.

[13] P. Jousset, T. Reinsch, T. Ryberg, H. Blanck, A. Clarke, R. Aghayev, *et al.*, "Dynamic strain determination using fibre-optic cables allows imaging of seismological and structural features," *Nature Communications*, 2018, 9(1): 2509.

[14] A. Sladen, D. Rivet, J. P. Ampuero, L. De Barros, Y. Hello, G. Calbris, *et al.*, "Distributed sensing of earthquakes and ocean-solid Earth interactions on seafloor telecom cables," *Nature Communications*, 2019, 10(1): 5777.

[15] E. F. Williams, M. R. Fernández-Ruiz, R. Magalhaes, R. Vanthillo, Z. Zhan, M. González-Herráez, *et al.*, "Distributed sensing of microseisms and teleseisms with submarine dark fibers," *Nature Communications*, 2019, 10(1): 5778.

[16] N. J. Lindsey, T. C. Dawe, and J. B. Ajo-Franklin, "Illuminating seafloor faults and ocean dynamics with dark fiber distributed acoustic sensing," *Science*, 2019, 366(6469): 1103–1107.

[17] S. Zhang, H. Li, C. Fan, Z. Zeng, C. Xiong, J. Wu, *et al.*, "Adaptive decentralized AI scheme for signal recognition of distributed sensor systems,"

Opto-Electronic Advances, 2024, 7(12): 240119.

[18] M. Mlejnek, J. D. Downie, and M. O'Sullivan, "Examination of potential terrestrial system effects from Raman pumps below cable cutoff in G.654.E fibers," *Journal of Lightwave Technology*, 2019, 37(17): 4282–4294.

[19] Z. N. Wang, J. J. Zeng, J. Li, M. Q. Fan, H. Wu, F. Peng, *et al*., "Ultra-long phase-sensitive OTDR with hybrid distributed amplification," *Optics Letters*, 2014, 39(20): 5866.

[20] A. Masoudi, M. Beresna, and G. Brambilla, "152 km-range single-ended distributed acoustic sensor based on inline optical amplification and a micromachined enhanced-backscattering fiber," *Optics Letters*, 2021, 46(3): 552.

[21] J. Li, B. Chang, J. Du, T. Tan, Y. Geng, H. Zhou, *et al*., "Coherently parallel fiber-optic distributed acoustic sensing using dual Kerr soliton microcombs," *Science Advances*, 2024, 10(3): eadf8666.

[22] J. Xiong, Z. Wang, Y. Wu, and H. Wu, "Long-distance distributed acoustic sensing utilizing negative frequency band," *Optics Express*, 2020, 28(24): 35844.

[23] M. Wang, J. Qu, S. Qu, W. Wang, S. Huang, W. Zhao, *et al*., "High spatial-resolved *Φ*-OTDR system based on differential pulse width sequence technique," *IEEE Photonics Technology Letters*, 2024, 36(6): 373–376.

[24] Z. Wang, Z. Pan, Z. Fang, Q. Ye, B. Lu, H. Cai, *et al*., "Ultra-broadband phase-sensitive optical time-domain reflectometry with a temporally sequenced multi-frequency source," *Optics Letters*, 2015, 40(22): 5192.

[25] D. Chen, Q. Liu, X. Fan, and Z. He, "Distributed fiber-optic acoustic sensor with enhanced response bandwidth and high signal-to-noise ratio," *Journal of Lightwave Technology*, 2017, 35(10): 2037–2043.

[26] D. Chen, Q. Liu, and Z. He, "108-km distributed acoustic sensor with 220-$\mathrm{p\varepsilon}/\sqrt{\mathrm{Hz}}$ strain resolution and 5-m spatial resolution," *Journal of Lightwave Technology*, 2019, 37(18): 4462–4468.

[27] H. Li, C. Fan, T. Liu, Y. Liu, Z. Yan, P. Shum, *et al*., "Time-slot multiplexing based bandwidth enhancement for fiber distributed acoustic sensing," *Science China Information Sciences*, 2022, 65(1): 119303.

[28] A. Wan, Y. Liang, Y. Wu, S. Zhang, Z. Ye, and Z. Wang, "Sensing bandwidth enlargement with orthogonal codes and mismatched filters in distributed acoustic sensing system," in *2024 22nd International Conference on Optical Communications and Networks*, Harbin, China, Jul. 26–29, 2024, pp. 1–3.

[29] D. Chu, "Polyphase codes with good periodic correlation properties (Corresp.)," *IEEE Transactions on Information Theory*, 1972, 18(4): 531–532.

[30] N. Zhang, G. Peng, H. Chen, and C. Tang, "PBN-CSMA/CA: a power back-off NOMA-based CSMA/CA Protocol for Ad Hoc networks," *IEEE Transactions on Mobile Computing*, 2025, 24(9): 7980–7993.

[31] S. Murano, C. Perez-Rubio, D. Gualda, F. J. Alvarez, T. Aguilera, and C. D. Marziani, "Evaluation of Zadoff-Chu, Kasami, and chirp-based encoding schemes for acoustic local positioning systems," *IEEE Transactions on Instrumentation and Measurement*, 2020, 69(8): 5356–5368.

[32] B. Han, H. Wu, Y. Liu, S. Dong, Y. Rao, Z. Wang, *et al*., "Ultralong single-ended random fiber laser and sensor," *Laser & Photonics Reviews*, 2023, 17(6): 2200797.

[33] C. Fan, H. Li, K. Zhang, H. Liu, Y. Sun, H. Liu, *et al*., "300 km ultralong fiber optic DAS system based on optimally designed bidirectional EDFA relays," *Photonics Research*, 2023, 11(6): 968–978.

[34] C. Gao, K. C. Teh, and A. Liu, "Piecewise nonlinear frequency modulation waveform for MIMO radar," *IEEE Journal of Selected Topics in Signal Processing*, 2017, 11(2): 379–390.

[35] J. Zhang, H. Wu, H. Zheng, J. Huang, G. Yin, T. Zhu, *et al*., "80 km fading free phase-sensitive reflectometry based on multi-carrier NLFM pulse without distributed amplification," *Journal of Lightwave Technology*, 2019, 37(18): 4748–4754.

[36] F. Berggren and B. M. Popović, "Permutation polynomial interleaved Zadoff-Chu sequences," *IEEE Transactions on Information Theory*, 2024, 70(8): 6068–6075.

[37] Y. Wakisaka, H. Takahashi, D. Iida, and Y. Koshikiya, "Broad-bandwidth and accurate optical vibration sensing by using FDM *Φ*-OTDR with linear regression analysis of multi-frequency phase responses," *Optics Express*, 2023, 31(17): 27990.

[38] Y. Li, H. Zhang, P. Wang, Y. Gao, Y. Wang, and B. Jin, "SNR enhancement for FDM phase-sensitive OTDR using phase-frequency modulation method," *Optics & Laser Technology*, 2025, 188: 112980.

[39] J. Ji, J. Chen, Z. Xiao, Z. Li, J. Zhang, S. Feng, *et al*., "High-fidelity frequency division multiplexed distributed acoustic sensor based on desynchronized dual-frequency-pulse sequence," *Journal of Lightwave Technology*, 2025, 43(18): 8981–8990.

[40] M. Wu, X. Fan, X. Zhang, L. Yan, and Z. He, "Frequency response enhancement of phase-sensitive OTDR for interrogating weak reflector array by using OFDM and Vernier effect," *Journal of Lightwave Technology*, 2020, 38(17): 4874–4882.